

Evolution of ferromagnetism captured by magnetotransport in compressively strained $\text{Sr}_{1-x}\text{Pb}_x\text{RuO}_3$ thin films

L.-F. Zhang^{1,*}, T. C. Fujita¹ and M. Kawasaki^{1,2}¹Department of Applied Physics and Quantum Phase Electronics Center, University of Tokyo, Tokyo 113-8656, Japan²RIKEN Center for Emergent Matter Science (CEMS), Wako 351-0198, Japan

(Received 5 February 2021; accepted 18 March 2021; published 2 April 2021)

A-site doping of SrRuO_3 (SRO) has revealed that the evolution of ferromagnetism in SRO cannot be explained only by the A-site ion radii. Recently, Pb^{2+} doping, which introduces a lone-pair-electrons on A-site, has been found to weaken the ferromagnetism dramatically, indicating that a hybridization between Ru-4d and Pb-6s orbitals would play an important role in this system. Here we perform magnetotransport measurements for single crystalline $\text{Sr}_{1-x}\text{Pb}_x\text{RuO}_3$ ($0 \leq x \leq 1$) thin films grown on SrTiO_3 (001) substrate for elucidating the change of electronic structure and ferromagnetism. Sign inversion of AHE typically observed in SRO disappears as doping Pb^{2+} , indicating a relationship between Weyl points and Fermi energy as suggested in previously reported Ca doped SRO system. Evidenced from longitudinal resistivity and Hall effect, ferromagnetic phase is weakened rapidly and vanishes at $x \approx 0.6$, which is in good agreement with bulk samples.

DOI: [10.1103/PhysRevMaterials.5.044402](https://doi.org/10.1103/PhysRevMaterials.5.044402)

I. INTRODUCTION

Transition metal (TM) perovskite oxide (ABO_3) is a rich platform of emergent physics because of the interplay among the charge, orbital, and spin degrees of freedom of electrons. In the 3d perovskite system, it is well known that the physical properties, such as magnetism and conductivity, are highly dependent on the bandwidth and filling of orbitals, which control the transfer integral and Coulomb interaction of electrons. For example, properties of LnNiO_3 (Ln : lanthanoid) can be well explained as a function of bandwidth. By changing A-site from Lu to La, the properties vary from antiferromagnetic insulator to metal. The main reason for this variation is the ion radii of A-site which affect the Ni-O-Ni bond angle and thus change the bandwidth [1].

In the 4d perovskite system, on the other hand, the well-established trend of physical properties for rather localized electrons in 3d TM cannot be readily applied because of the itinerant electrons originating from more extended 4d orbitals. One typical example is SrRuO_3 (SRO), which is understood as a typical itinerant ferromagnetic (FM) oxide with magnetic transition temperature (T_C) of 160 K. Perovskite ruthenates (ARuO_3) with the same Ru^{4+} ion as SRO, CaRuO_3 (CRO), and BaRuO_3 (BRO) are widely studied as well. Comparing these three compounds, since all of Ca^{2+} (1.34 Å), Sr^{2+} (1.44 Å), and Ba^{2+} (1.61 Å) have closed shell electron configuration, ion radii, which determine the distortion of RuO_6 octahedra and thus vary the bandwidth, may be regarded as the decisive factor to affect the FM state in ARuO_3 . However, in the series of Ba^{2+} and Ca^{2+} doping into SRO, SRO has the highest T_C ; meanwhile, CRO is paramagnetic and BRO is FM with T_C of 80 K, indicating the FM phase cannot be

explained simply by ion radii [2], as discussed later in Fig. 6. Jin *et al.* has experimentally studied the reason for suppression of the FM phase [3]. Besides the ion radii, they suggest that the local stress effect on Ru-O bond may play a significant role. In Ca and Ba doping, compressive and stretching stress are observed, respectively, both of which results in a lower T_C . In addition, an unconventional anomalous Hall effect (AHE) is observed for SRO, which is not proportional to magnetization accompanied with sign inversion. From this behavior, the role of Weyl points, which are the crossing points of dispersion curves, has been revealed as a source of topological Hall effect [4].

Because of these interesting properties related to magnetism, A-site doping has been further examined to clarify the origin and the structural dependence of the FM phase in SRO. For smaller dopant, not only bulk polycrystalline samples but also thin films of $\text{Sr}_{1-x}\text{Ca}_x\text{RuO}_3$ (SCRO) were synthesized [5–9]. In thin film samples, due to the epitaxy technique, it is easier to obtain a single crystalline sample which is necessary to perform magnetotransport measurements, enabling the discussion of modulation in electronic structure. Interestingly, the sign inversion of AHE in SCRO shifts to lower temperature as x increases and totally disappears at $x \geq 0.4$, indicating a variance in its electronic structure [5]. However, for larger dopant, although bulk polycrystalline samples were synthesized by high-pressure synthesis, cubic perovskite phase of BRO is challenging to grow in thin-film form because of the competition with a more stable hexagonal phase [3,10]. Another possible option is Pb^{2+} (1.49 Å) whose ion radius is between those of Sr^{2+} and Ba^{2+} . A series of $\text{Sr}_{1-x}\text{Pb}_x\text{RuO}_3$ (SPRO) have already been studied in bulk polycrystalline samples fabricated by high-pressure synthesis [11]. Surprisingly, although Pb^{2+} is much smaller than Ba^{2+} , the FM phase diminishes more rapidly and disappears at about $x = 0.6$, while BRO is FM metal as seen in Fig. 6(b). As a

*Corresponding: zhang@kws.k.u-tokyo.ac.jp

reason for this phenomena, the effect of lone-pair-electrons in Pb^{2+} , which is absent in Ba^{2+} , was suggested to play a significant role. Since only polycrystalline SPRO has been synthesized so far, its magnetotransport properties have been unknown. Because sign reversal of AHE has been observed in SCRO, it is intriguing to examine how AHE evolves in SPRO during a process of losing FM phase. In our pervious report, we have already succeeded in fabricating PbRuO_3 (PRO) epitaxial thin films on various substrates and observed a metallic ground state with a possibly anti-FM fluctuation [12]. In this report, in order to reveal the change in electronic and magnetic properties in SPRO, we have fabricated whole series of single crystalline SPRO thin films and performed magnetotransport measurements.

II. EXPERIMENT

Series of single crystalline SPRO thin films were prepared on SrTiO_3 (STO) (001) substrates by pulsed laser deposition (PLD). Several targets with $x = 0.5$ to 1 were prepared by solid-state reaction using PbO , SrCO_3 , and RuO_2 as starting materials. Nominal compositions of the powders ($0.5 \leq x \leq 1$) were mixed, milled, and calcined for 12 h at 800°C . Then, the products were milled again, pressed to pellets, and sintered for 24 h at 1100°C . The structural properties of the targets were characterized by powder XRD, confirming that a mixture of pyrochlore $\text{Pb}_2\text{Ru}_2\text{O}_{6.5}$ and perovskite SrRuO_3 was formed. A commercialized sintered target (Toshiba Co. Ltd.) was employed for SRO ($x = 0$). Before deposition, STO substrate was annealed *in situ* at 950°C under 10^{-5} Torr oxygen to obtain a clear step-terrace structure with single-unit-cell height. For SPRO films ($0 < x \leq 1$), the deposition was conducted at a substrate temperature of 450°C and an oxygen pressure of 0.1 mTorr. KrF excimer laser ($\lambda = 248$ nm) with a pulse frequency of 1 Hz and fluence of ≈ 2 J/cm² were employed to ablate the targets. The growth conditions are the same as those for PRO, since PRO is a metastable phase and its growth condition is more rigorous than that of SRO [12]. SRO film ($x = 0$) was grown under the previously reported conditions [13].

Structural properties of the samples were characterized by x ray diffraction (XRD) (Smart Lab, Rigaku) at room temperature. XRD measurements confirmed that, in present study, thicknesses of the doped films ($0 < x < 1$) ranged from 12 to 17 nm, and those for SRO ($x = 0$) and PRO ($x = 1$) film are 26 and 7 nm, respectively. Reciprocal space mappings (RSM) ensured that all films were coherently grown and in-plane lattice constant was identical to that of STO substrate. Together with 2θ - ω scans along [001] direction of STO, which are discussed later, all films were proved to have a pseudocubic structure.

Magnetotransport measurements were performed by a 9 T superconducting magnet equipped with a liquid He cryostat (PPMS, Quantum Design Co.). The films were cut into a rectangular shape with a typical size of 2×5 mm², and aluminum wire was attached to the films at six points to obtain longitudinal (ρ_{xx}) and Hall (ρ_{yx}) resistivities by four-terminal measurements. Magnetic field was applied perpendicularly to the film; ρ_{xx} and ρ_{yx} are deduced by a conventional symmetrization and antisymmetrization procedures, respectively.

III. RESULTS AND DISCUSSION

Magnified XRD 2θ - ω scans around (002) (pseudocubic setting) peak of SPRO thin films are presented in Fig. 1(a), where the (002) peaks of SPRO films are indicated by triangles, and they shift from low to high 2θ angle as Pb concentration in the target decreases. In Fig. 1(b), lattice constants of CRO, SRO, PRO (pseudo-cubic settings), BRO, and STO are presented for a better understanding of the epitaxial relationship of representative perovskite ruthenates [2,11]. Because lattice constants of SPRO are larger than that of STO substrate, all the samples in this study are grown under compressive strain.

Then, we discuss the composition of the films. Since perovskite PRO is a metastable phase and chemically unstable and PbO has high vapor pressure, SRO would be preferentially crystallized even by using the SPRO targets. In addition, as we have already reported [12], the growth window of PRO is quite narrow. Therefore, only a slight deviation in growth temperature may lead to the significant deficiency of Pb, especially under coexistence of Sr. Hence, a difference between nominal target composition and actual film composition should be examined. In order to estimate the actual composition of the films, we have performed an energy dispersive x ray spectroscopy with scanning electron microscope (SEM-EDX), for which the electron beam is parallel to the surface normal. Because STO substrate is employed, the Pb/Sr ratio cannot be directly measured by SEM-EDX in this configuration. However, assuming that the A- and B-site cation ratio is unity, the Pb/Ru ratio can be estimated. The result of composition with lattice constant is shown in Fig. 1(c). This clearly indicates that the actual Pb concentration in the films is much less than the nominal target compositions. Because all the films are fully strained on the STO substrates, we can also deduce out-of-plane lattice constants with Vegard's law, as shown in Fig. 1(c). One can see the general tendency that the lattice constants are bigger than those calculated from Vegard's law. This might be explained by lattice expansion originating from off-stoichiometry or oxygen deficiency, but these are challenging to distinguish in this study. Summarizing above, although it is difficult to obtain the accurate composition of the films, we have confirmed that Pb doping concentration x systematically varies from 0 to 1. Therefore, each sample is annotated by the chemical composition deduced from SEM-EDX hereinafter.

As presented in Figs. 2(a) and 2(b), all the films have the same order of ρ_{xx} at 300 K and ρ_{xx} exhibits metallic temperature dependence down to 2 K. In Fig. 2(a), kinks in ρ_{xx} - T curves are observed for $x \leq 0.33$ films, which conventionally appear in FM materials at T_C . The magnetic transition is more clearly seen in the temperature derivative of ρ_{xx} presented in Fig. 2(c): $T_C = 136, 128, 123, 73,$ and 68 K for $x = 0, 0.06, 0.11, 0.24,$ and 0.33 , respectively. It is clear that T_C decreases as Pb concentration increases. From these results, films with $x \leq 0.33$ are suggested to be FM. In addition, as we will discuss later, from AHE, $x = 0.42$ and 0.63 films are also suggested to be FM with $T_C \approx 35$ and 4 K, respectively.

Now, we discuss the magnetotransport properties of SPRO films. Hereinafter, we refer to $x = 0.06, 0.11$ as light doped samples; $x = 0.24, 0.33,$ and 0.42 as middle doped samples;

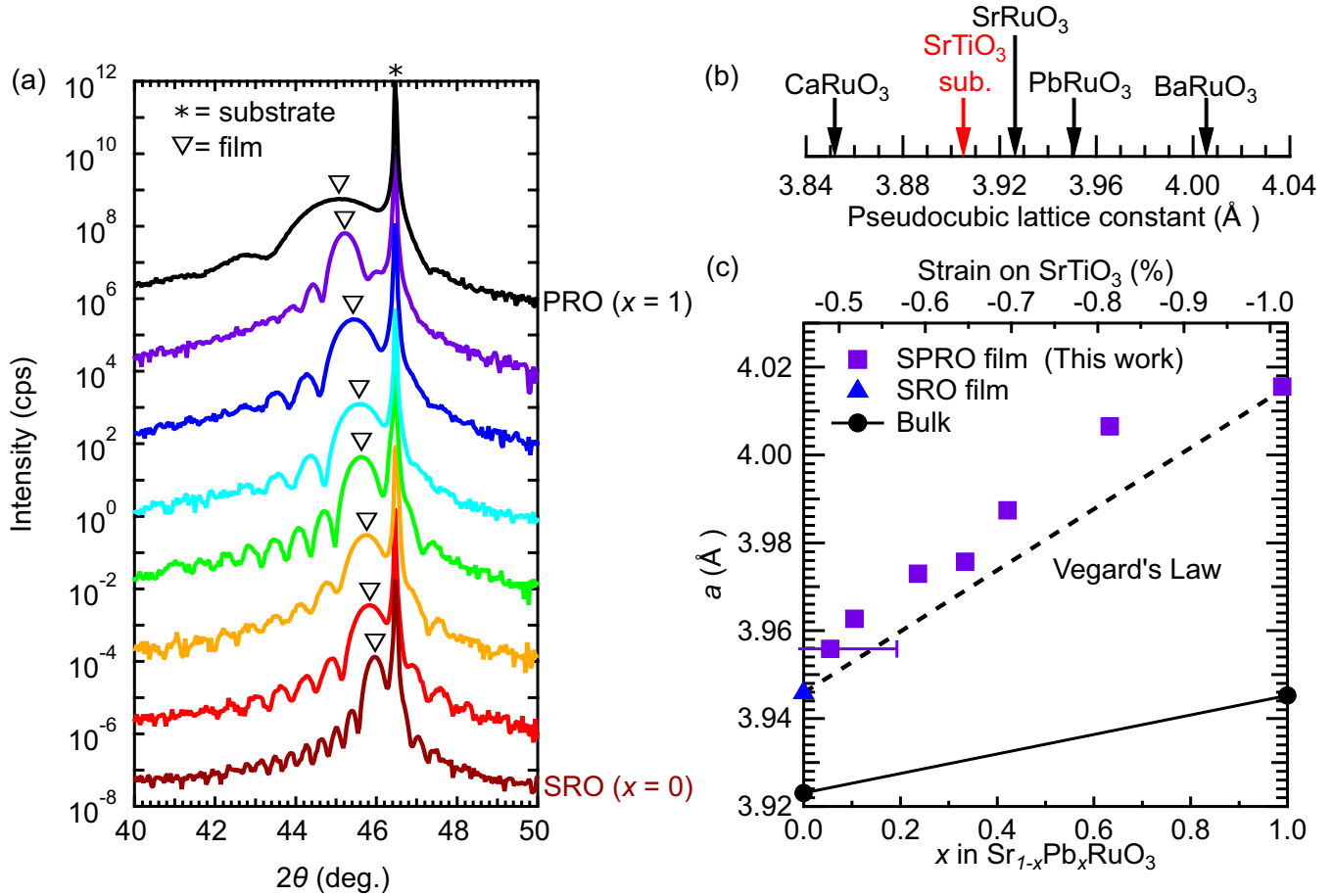


FIG. 1. (a) The XRD 2θ - ω scans of $\text{Sr}_{1-x}\text{Pb}_x\text{RuO}_3$ films grown on STO (001) substrates around pseudocubic (002) peak. Peaks of STO and films are indicated by an asterisk and triangles, respectively. (b) Comparison of pseudocubic lattice constants of CRO, SRO, PbRuO_3 , BRO, with STO substrate [2,11]. (c) Out-of-plane lattice constant taken from $(002)_{pc}$ peak as a function of the Pb concentration x deduced by SEM-EDX analysis. The Vegard's law, interpolated between the data for SRO taken from [19] and PbRuO_3 from this work, is indicated with the broken line. Pseudocubic lattice constants (black circles) for SRO [20] and PbRuO_3 [21] bulk crystals, which are calculated from $a_{pseudocubic} = (V_{ortho}/4)^{1/3}$, are also shown.

$x = 0.63$ as heavy doped sample. In Figs. 3 and 4, those groups are distinguished by open circles, open circles with a cross inside, and closed circle symbols, respectively.

Temperature dependence of the magnetoresistance (MR) ratio at $B = 9$ T $\{[\rho_{xx}(9\text{ T})/\rho_{xx}(0) - 1] \times 100\}$, presented in Fig. 3, also supports the decay of FM as x increases. One can see that samples with $x \leq 0.42$ show minima in MRR, as indicated by triangles, at the temperature slightly above the T_C deduced from $\rho_{xx}-T$. This kind of minima is generally observed in FM materials. When it is close to the FM phase transition, magnetic field can induce a FM order, resulting in suppression of spin fluctuation, which leads to less magnetic scattering on conduction electrons and stronger negative MR. Therefore, the minima in Fig. 3 suggests the presence of FM phase in $x \leq 0.42$ samples and the shift of the minima indicating that Pb doping weakens the FM. On the other hand, heavy doped sample ($x = 0.63$) shows almost indiscernible MR as PRO, indicating that FM phase almost disappears.

Next, we discuss the Hall effect, which contains the information about carrier density and magnetic properties. The magnetic field dependence of Hall resistivity is presented in Fig. 4. Here, we show representative data of $x = 0.06$ for light

doped sample, $x = 0.42$ for middle doped sample, $x = 0.63$ for heavy doped sample, and $x = 1$ for PRO. To evaluate the $\rho_{yx}-B$ curves, we separate Hall effect into ordinary Hall effect (OHE) and AHE. Generally, ρ_{yx} can be expressed as

$$\rho_{yx} = R_H B + \rho_{AHE}. \quad (1)$$

The first term corresponds to the ordinary Hall term, and the second term is the anomalous Hall term that is generally proportional to magnetization (M). From Eq. (1), the Hall resistivity is supposed to be proportional to B at high magnetic field where M saturates. However, in perovskite ruthenates, such as SCRO [8], ρ_{yx} is not linear even at 9 T. In our SPRO films, the high field Hall effect resistivity is not totally proportional to B , either. Therefore, in order to discuss the trend of the $\rho_{yx}-B$ curves qualitatively, we deduce R_H by a linear fitting of $\rho_{yx}-B$ curves between $B = 7$ and 9 T. On the other hand, the value of ρ_{yx} at $B = 0$ T, where the contribution of OHE is 0, is employed for the evaluation of anomalous Hall resistivity (ρ_{AHE}). It should be noted that, under this definition, only AHE originating from the FM phase can lead to nonzero ρ_{yx} at $B = 0$ T as a result of FM spontaneous magnetization. Here, in order to evaluate AHE, we employed the anomalous

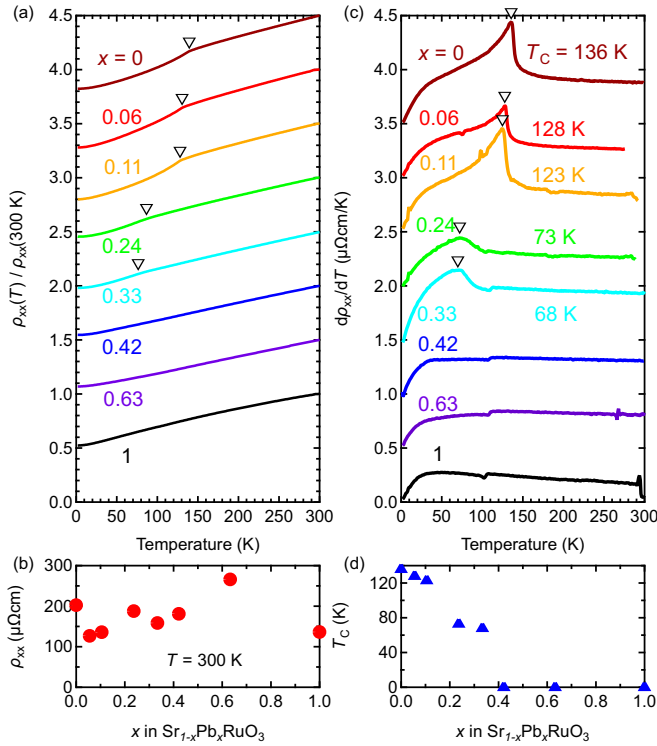


FIG. 2. (a) Temperature dependence of normalized longitudinal resistivity $[\rho_{xx}(T)/\rho_{xx}(300\text{ K})]$ for the series of $\text{Sr}_{1-x}\text{Pb}_x\text{RuO}_3$ films with a vertical offset of 0.5 for $x < 1$. (b) The resistivities at $T = 300\text{ K}$ of each film. (c) Temperature derivative of resistivities with a vertical offset of $0.5\ \mu\Omega\text{cm}/\text{K}$. In (a) and (c), magnetic transition points (T_C) are indicated by open triangles. The transition temperatures estimated from the points are shown near each curve. (d) The x dependence of T_C .

Hall angle, which is defined as

$$\sigma_{\text{AHE}}/\sigma_{xx} = \rho_{\text{AHE}} \times \rho_{xx}/(\rho_{\text{AHE}}^2 + \rho_{xx}^2). \quad (2)$$

Temperature dependence of Hall coefficient R_H and anomalous Hall angle is presented in Figs. 5(a) and 5(b), respectively. In Fig. 5(a), SRO ($x = 0$) shows a peak and a sign change above T_C . Similar structures are observed for $x \leq 0.42$

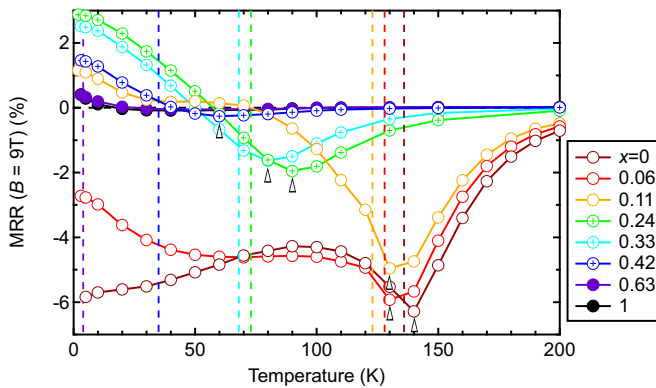


FIG. 3. Temperature dependence of MRR at $B = 9\text{ T}$ for the series of $\text{Sr}_{1-x}\text{Pb}_x\text{RuO}_3$ films. Minima of each curve are indicated by triangles. T_C for each sample are indicated by dashed lines in corresponding colors.

samples around their T_C , indicating a correlation with FM phase as reported in SRO [14]. Since the information of carrier density can be obtained from R_H , they suggested a coexistence of two types of carriers, the so-called multicarrier behavior, in SRO. Assuming the presence of multiband near Fermi energy, a band splitting originating from FM phase may account for the sign inversion of R_H .

In Fig. 5(b), SRO ($x = 0$) and light doped samples ($x \leq 0.11$) show a sign change of AHE below T_C , which is absent in middle doped samples ($x = 0.24, 0.33, 0.42$). Interestingly, these behaviors in AHE are similar to those in SCRO thin films as reported by Mathieu *et al.* [5]. By assuming the presence of band crossing, the so-called Weyl point [15], they utilized first-principle calculation to successfully reproduce the nonmonotonous and nontrivial relationship between anomalous Hall conductivity and M . According to their theory, the Berry phase originating from Weyl points plays an essential role in sign inversion of AHE [16]. In the FM state, when M changes, the Fermi energy crosses Weyl points, and the Berry phase contributes to AHE and results in sign inversion. In our SPRO films, it is supposed to have a similar relationship between them. When Pb doped, the saturate M is suppressed, and the sign inversion disappears consequently as in the case of SCRO.

Furthermore, from the Hall effect, the information about magnetic transition can be deduced. As mentioned earlier, AHE is generally proportional to M . Therefore, hysteresis loops in magnetic field dependence of ρ_{yx} is evidence of a FM phase. T_C can be determined by the temperature at where the hysteresis loop is observed for the first time when decreasing the temperature. For example, in Fig. 4(b), the hysteresis loop appears at $T = 30\text{ K}$, indicating that T_C is between $T = 30$ and 40 K . T_C deduced from the Hall effect is shown in Fig. 6(a) with a comparison of those deduced from kink in $\rho_{xx}-T$. From Fig. 6(a), T_C deduced from the Hall effect and $\rho_{xx}-T$ are always consistent. This guarantees the validity of T_C deduced from $\rho_{xx}-T$ curves in Fig. 2(a). For $x = 0.42$ and 0.63 samples, although kink is not observed in $\rho_{xx}-T$, hysteresis loops in ρ_{yx} are observed under $T = 30$ and 3 K , respectively, which prove the existence of the FM phase. It will be worth mentioning that ρ_{yx} shows nonlinear magnetic field dependence even above T_C determined by our manner, although it does not have hysteresis at that temperature region. This kind of behavior has been reported in previous studies and possibly originates from multiband effect. Yet, T_C determined by $M-T$ measurements shows good agreement with the temperature at which ρ_{yx} starts to exhibit hysteresis [8]. Therefore, our way of determining T_C will be pretty reasonable.

Finally, we review a phase diagram of A-site doped SRO system ($\text{Sr}_{1-x}\text{A}_x\text{RuO}_3$: $A = \text{Ca}^{2+}, \text{Pb}^{2+}, \text{and Ba}^{2+}$) as shown in Fig. 6(b). Here, bulk and film samples [on STO (001) substrate] for Ca and Pb doped and bulk samples for Ba doped SRO are shown [2,6,17]. In bulk samples, starting from SRO with the highest T_C of 160 K , A-site doping results in reduction of T_C regardless of the ionic radii of the dopants. We remind that the ion radii of $\text{Ca}^{2+}, \text{Sr}^{2+}, \text{Pb}^{2+}, \text{and Ba}^{2+}$ are $1.34\ \text{\AA}, 1.44\ \text{\AA}, 1.49\ \text{\AA}, \text{and } 1.61\ \text{\AA}$, respectively. Among these three dopants ($\text{Ca}^{2+}, \text{Pb}^{2+}, \text{and Ba}^{2+}$), Pb^{2+} has the closest ion radius to Sr^{2+} , thus we can naturally expect that the Pb doping effect will be less effective than others if only ionic radii are

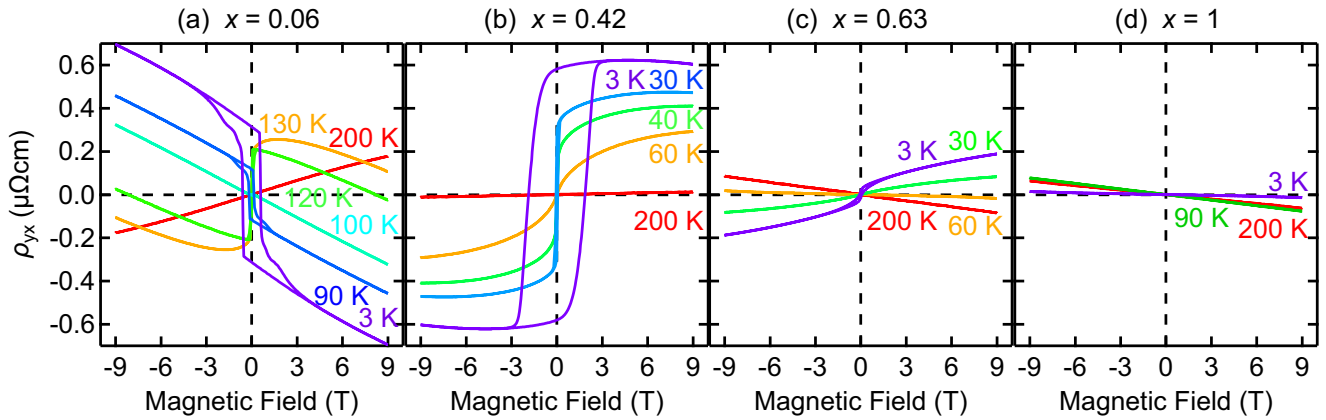


FIG. 4. Magnetic field dependence of Hall resistivity for the film with (a) $x = 0.06$, (b) 0.42 , (c) 0.63 , and (d) 1 at several temperatures.

considered. In Pb^{2+} doped samples, however, the FM phase disappears at about $x \approx 0.6$. This has been explained by the unique electron configuration of Pb^{2+} , namely, the presence of a lone-pair electrons on $6s$ orbital. These $6s$ lone-pair electrons hybridize with Ru- $4d$ orbit, introducing a further distortion in RuO_6 octahedra, leading to the disappearance of the FM phase [11,18].

Then, we compare bulk and our film of SPRO samples. In our thin film samples, from Fig. 4(b), AHE in the $x = 0.63$

sample is negligibly small, indicating this sample is very close to critical point. Considering our experiment accuracy, it is in good agreement with the phase boundary of $x \approx 0.6$ which has been reported in bulk samples [11]. Meanwhile, T_C of films is always lower than those of bulk samples for similar doping level x . This is clearly different from SCRO samples. T_C for film samples is lower than that of bulk samples at lower doping level, but it becomes higher at higher doping level. This can be explained in terms of lattice distortion arising from the compressive epitaxial strain as already shown in Fig. 1(b). As theoretically suggested by Lu *et al.* [18], when Pb is doped into SRO, the reduction of T_C is partly ascribed to the Jahn-Teller distortion. According to their calculation, the ab-plane of RuO_6 octahedra is compressed by Pb doping, and the $4d^4$ electrons of Ru^{4+} tend to fully occupy doubly degenerated lower d_{zx} and d_{yz} orbitals, which lead to a less magnetic moment and hence weaken the FM phase. Therefore, the compressive strain in our films can be the origin of the reduction of T_C . On the other hand, in the case of SCRO, the crossover occurs at $x \approx 0.6$, where the lattice constant becomes identical to that of STO substrate and hence the epitaxial strain changes from compressive to tensile.

In conclusion, we have fabricated single crystalline SPRO thin films by PLD to investigate magnetotransport properties. Evidenced by both longitudinal and Hall resistivities, evolution of the FM phase is observed. The FM phase disappears at $x \approx 0.6$ while T_C is always lower than that of bulk samples, which plausibly originates from compressive strain from STO substrate. Sign reversal of anomalous Hall conductivity is suppressed by increasing the doping level as in the case of previously reported SCRO. These findings will endow perovskite ruthenates, which have been gathering attention for decades, with further controllability of their properties and functionalities.

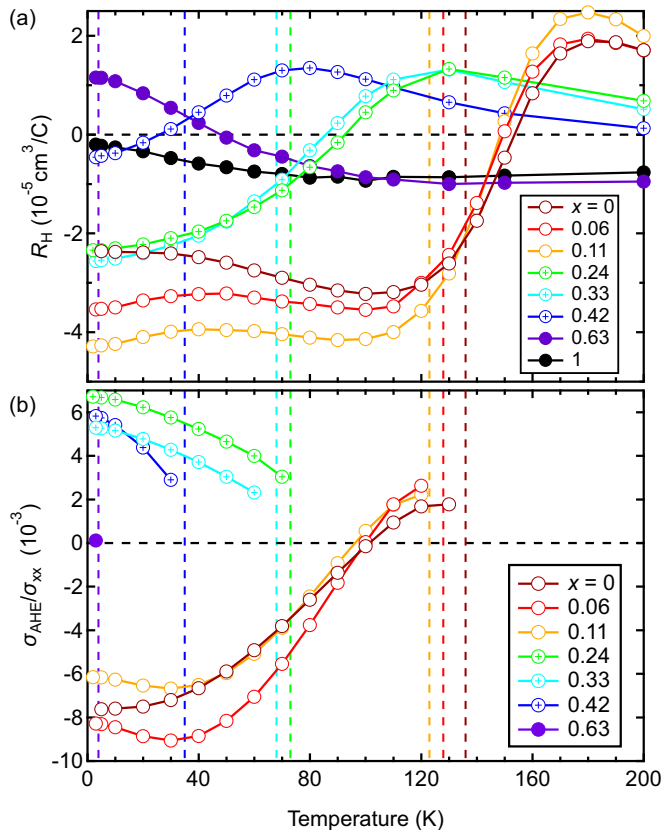


FIG. 5. Temperature dependence of (a) Hall coefficient R_H and (b) anomalous Hall angle $\sigma_{\text{AHE}}/\sigma_{xx}$ for the series of $\text{Sr}_{1-x}\text{Pb}_x\text{RuO}_3$ films. See the main text for the definition of R_H and anomalous Hall angle. T_C for each sample are indicated by dashed lines in corresponding colors.

ACKNOWLEDGMENTS

This work was supported by the Japan Science and Technology Agency Core Research for Evolutional Science and Technology (JST CREST) (Grant No. JPMJCR16F1) and by JSPS Grant-in-Aid for Early-Career Scientists No. JP20K15168.

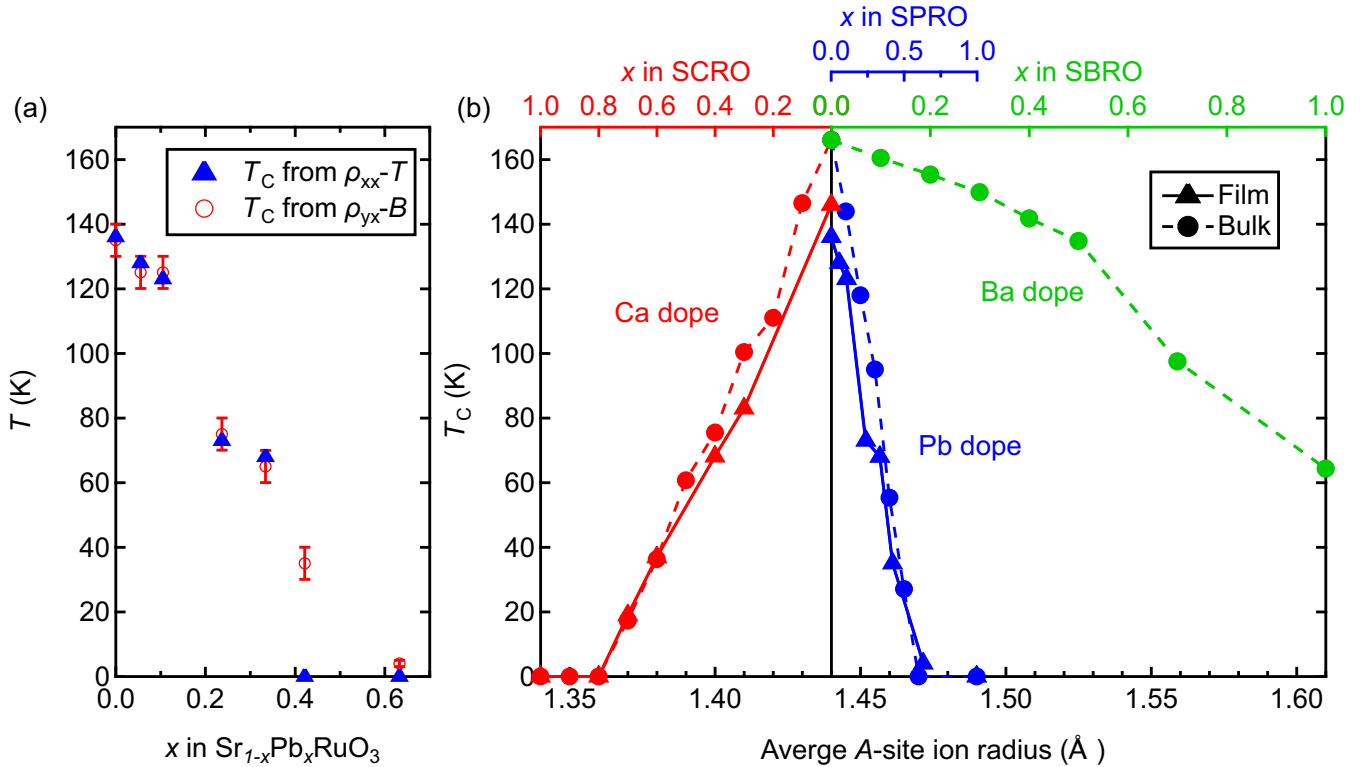


FIG. 6. (a) Comparison between the transition temperature deduced from the kink of $\rho_{xx}-T$ [Fig. 2(c)] and the magnetic field dependence of the Hall effect (Fig. 4). (b) Magnetic phase diagram for series of $\text{Sr}_{1-x}\text{A}_x\text{RuO}_3$ ($A = \text{Ba}, \text{Ca}, \text{Pb}$). In Ca doped and Pb doped series, both bulk (solid line) and film (dashed line) data are shown. The data are taken from publications for Ca doped bulk [2], Ca doped film [6], Ba doped bulk [2], and Pb doped bulk samples [11].

- [1] M. Imada, A. Fujimori, and Y. Tokura, *Rev. Mod. Phys.* **70**, 1039 (1998).
- [2] J. G. Cheng, J. S. Zhou, and J. B. Goodenough, *Proc. Nat. Acad. Sci. USA* **110**, 13312 (2013).
- [3] C. Q. Jin, J. S. Zhou, J. B. Goodenough, Q. Q. Liu, J. G. Zhao, L. X. Yang, Y. Yu, R. C. Yu, T. Katsura, A. Shatskiy, and E. Ito, *Proc. Nat. Acad. Sci. USA* **105**, 7115 (2008).
- [4] G. Koster, L. Klein, W. Siemons, G. Rijnders, J. S. Dodge, C. B. Eom, D. H. A. Blank, and M. R. Beasley, *Rev. Mod. Phys.* **84**, 253 (2012).
- [5] R. Mathieu, A. Asamitsu, H. Yamada, K. S. Takahashi, M. Kawasaki, Z. Fang, N. Nagaosa, and Y. Tokura, *Phys. Rev. Lett.* **93**, 016602 (2004).
- [6] M. Wissinger, D. Fuchs, L. Dieterle, H. Leiste, R. Schneider, D. Gerthsen, and H. V. Löhneysen, *Phys. Rev. B: Condens. Matter Mater. Phys.* **83**, 144430 (2011).
- [7] P. Khalifah, I. Ohkubo, H. M. Christen, and D. G. Mandrus, *Phys. Rev. B: Condens. Matter Mater. Phys.* **70**, 134426 (2004).
- [8] P. Khalifah, I. Ohkubo, B. C. Sales, H. M. Christen, D. Mandrus, and J. Cerne, *Phys. Rev. B: Condens. Matter Mater. Phys.* **76**, 054404 (2007).
- [9] D. Fuchs, C. L. Huang, J. Schmalian, M. Wissinger, S. Schuppler, K. Grube, and H. V. Löhneysen, *Eur. Phys. J.: Spec. Top.* **224**, 1105 (2015).
- [10] N. Fukushima, K. Sano, T. Schimizu, K. Abe, and S. Komatsu, *Appl. Phys. Lett.* **73**, 1200 (1998).
- [11] J. G. Cheng, J. S. Zhou, and J. B. Goodenough, *Phys. Rev. B: Condens. Matter Mater. Phys.* **81**, 134412 (2010).
- [12] T. C. Fujita, L. F. Zhang, and M. Kawasaki, *Phys. Rev. Mater.* **4**, 031401(R) (2020).
- [13] T. Ohnishi and K. Takada, *Appl. Phys. Express* **4**, 025501 (2011).
- [14] S. C. Gausepohl, M. Lee, R. A. Rao, and C. B. Eom, *Phys. Rev. B: Condens. Matter Mater. Phys.* **54**, 8996 (1996).
- [15] Z. Fang, N. Nagaosa, K. S. Takahashi, A. Asamitsu, R. Mathieu, T. Ogasawara, H. Yamada, M. Kawasaki, Y. Tokura, and K. Terakura, *Science* **302**, 92 (2003).
- [16] N. Nagaosa, J. Sinova, S. Onoda, A. H. MacDonald, and N. P. Ong, *Rev. Mod. Phys.* **82**, 1539 (2010).
- [17] J. G. Cheng, J. S. Zhou, J. B. Goodenough, and C. Q. Jin, *Phys. Rev. B: Condens. Matter Mater. Phys.* **85**, 184430 (2012).
- [18] H. S. Lu and S. Ju, *Appl. Phys. Lett.* **98**, 122503 (2011).
- [19] W. Siemons, G. Koster, A. Vailionis, H. Yamamoto, D. H. A. Blank, and M. R. Beasley, *Phys. Rev. B: Condens. Matter Mater. Phys.* **76**, 075126 (2007).
- [20] C. W. Jones, P. D. Battle, P. Lightfoot, and W. T. A. Harrison, *Acta Crystallogr., Sect. C* **45**, 365 (1989).
- [21] J. G. Cheng, J. S. Zhou, and J. B. Goodenough, *Phys. Rev. B: Condens. Matter Mater. Phys.* **80**, 174426 (2009).